Annular two-phase flow in vertical smooth and corrugated pipes

van Eckeveld, A. C.; Gotfredsen, E.; Westerweel, J.; Poelma, C.

DOI
10.1016/j.ijmultiphaseflow.2018.07.004

Publication date
2018

Document Version
Final published version

Published in
International Journal of Multiphase Flow

International Journal of Multiphase Flow 109 (2018) 150–163

Contents lists available at ScienceDirect

International Journal of Multiphase Flow

journal homepage: www.elsevier.com/locate/ijmulflow

Annular two-phase flow in vertical smooth and corrugated pipes

A.C. van Eckeveld[a,*], E. Gotfredsen[b], J. Westerweel[a], C. Poelma[a]

[a] Delft University of Technology, Leeghwaterstraat 21, Delft, 2628CA, The Netherlands
[b] Technical University of Denmark, Nils Koppels Allé, Building 403, Kgs. Lyngby, 2800, Denmark

ARTICLE INFO

Article history:
Received 26 April 2018
Revised 25 June 2018
Accepted 2 July 2018
Available online 1 August 2018

ABSTRACT

Two-phase flow in ribbed or corrugated pipes is of interest in many industrial applications. Experiments are performed to assess the flow regime characteristics in upward annular flow through vertical smooth and corrugated pipes. From high speed recordings, the flow regime and temporal film characteristics are obtained. A novel implementation of a planar laser-induced fluorescence (PLIF) method is used to measure the film thickness, preventing strong reflections from deteriorating the measurements. Liquid accumulation between the ribs of the corrugated pipe is also measured using a PLIF technique. Furthermore, droplet sizing is performed combining shadowgraphic and interferometric techniques to capture a large droplet size range. The measurements show that the presence of pronounced corrugations at the pipe wall causes a strong increase in entrainment of liquid into the gas flow. The entrainment is correlated to the filling of the corrugations with liquid; it is significantly reduced (from 90% entrainment to 50%) when the corrugations are entirely filled with liquid. The amount of liquid filling of the corrugations is related to the superficial liquid film flow velocity. The liquid filling fraction (α) scales with the Weber and liquid Reynolds number, and the obtained scaling also holds when the experiments are repeated with a different liquid (mono-ethylene glycol) and with a larger corrugation geometry. Droplets occurring in corrugated pipe flow are 30–50% larger compared to the smooth pipe, as a consequence of the locally (at the locations of the cavities) increased film thickness.

1. Introduction

Ribbed or corrugated pipes are used in many industrial applications. They are for example applied as flexible flowlines and risers in the oil and gas industry. Other applications are primarily found in processing units in production plants (e.g. food and chemical industry), where heat and mass transfer are important. Axisymmetric or helical inserts have been shown to increase heat and mass transfer coefficients drastically under certain conditions. In many of these applications two-phase flows occur, having a low liquid loading. There is, however, limited understanding of the effect of ribs and corrugations on the flow regimes occurring in two-phase flows through these pipes. This work aims at contributing to this knowledge. Experiments are carried out to investigate the two-phase flow behavior in smooth and corrugated vertical pipes, operating in the annular flow regime. In this regime, a thin film transports a part of the liquid along the pipe wall. Liquid entrainment from the film into the gas core results in a fraction of the total liquid flow rate being transported as droplets.

Co-current two-phase flow in smooth vertical pipes has been subject of many studies. Azzopardi (1997) provides a thorough summary of this work. More recent contributions are provided by e.g. Belt et al. (2010); van 't Westende et al. (2007), and Sawant et al. (2008, 2009). In literature, the occurrence of upward annular flow is related to either the ability to suspend the dispersed phase (Turner et al., 1969) or the stability of the film at the wall (Zabaras et al., 1986). Either way, there exists a critical gas flow velocity below which the film is not sustained and a transition to churn flow is observed. For pipes with a 50 mm inner diameter, this critical gas flow velocity is approximately 14 m/s (Taitel et al., 1980). Pressure drop, entrainment ratio, void fraction and wave characteristics in vertical annular flow are reasonably well understood. For very low liquid flow rates, a full film is not sustained: the film breaks up and liquid is transported in rivulets along the pipe wall (Hewitt, 1965). For higher liquid flow rates, the full film is mainly characterized by two types of waves: capillary ripples and disturbance or roll waves (Azzopardi, 1997). Disturbance waves are the main source of liquid entrainment into the gas core (Arnold and Hewitt, 1967; Cousins and Hewitt, 1968; Azzopardi and Whalley, 1980). The inception of disturbance waves is therefore an important parameter when studying liquid entrainment in annular pipe flow. Azzopardi (1997) is one of various other authors proposing

* Corresponding author.
E-mail address: a.c.vaneckeveld@tudelft.nl (A.C. van Eckeveld).

https://doi.org/10.1016/j.ijmultiphaseflow.2018.07.004
0301-9322/

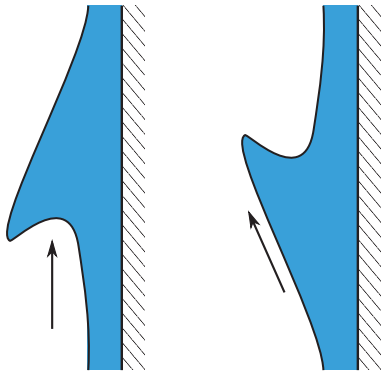

Fig. 1. Schematic representation of the two main droplet formation mechanisms in upward annular smooth pipe flow: bag break-up (left) and ligament break-up (right).

a criterion for the inception of disturbance waves, below which no significant entrainment is expected. According to Ishii and Grolmes (1975), entrainment is suppressed if the film Reynolds number[1] is smaller then 160, due to the absence of disturbance waves. Sawant et al. (2009) showed that the presence of disturbance waves is a necessary condition for the onset of entrainment, but not sufficient in itself. Especially at lower gas flow rates disturbance waves can occur without significant entrainment.

Two mechanisms for droplet formation from disturbance waves have been identified (Azzopardi, 1997). Fig. 1 gives a schematic representation of these two mechanisms. At lower gas and liquid flow rates, the bag break-up mechanism is dominant. Part of the wave is undercut by the gas flow, resulting in the formation of droplets. The second mechanism, occurring at higher gas flow speeds, is the ligament break-up mechanism, where a ligament is sheared from the waves by the high speed gas phase. This mechanism occurs over a large range of operating parameters. Several studies aimed to model the entrainment rate in annular pipe flow. Ishii and Mishima (1989) used the onset of entrainment criterion developed by Ishii and Grolmes (1975), to come up with an entrainment correlation. The correlation is based on the assumption that the excess liquid, above the entrainment onset limit, is entrained into the gas flow. They found a liquid Reynolds number dependency in the transition regime ($160 < Re_f < 1635$), and also introduced a viscosity dependency. This viscosity dependency is not warranted according to Wallis (1968). Pan and Hanratty (2002) developed a similar correlation, without the liquid Reynolds number and viscosity dependency.

The influence of non-smooth pipe walls on the two-phase flow is less well understood, but very relevant in certain applications, such as corrugated risers (Belfroid et al., 2013), ribbed wall heat exchangers for boiling and condensation (Agarwal and Rao, 1996), and mass transfer applications (Kukreja et al., 1993). Two-phase flow in corrugated pipes is mainly studied in the context of internal helical wires or other types of inserts in smooth pipes. Heat transfer coefficients can be significantly increased when these type of inserts are used. This behavior, however, is strongly dependent on the appearing two-phase flow regime. Several studies are devoted to the flow regime boundaries in two-phase flows through pipes with inserts. Agarwal and Rao (1996) found a significant increase of the heat transfer coefficients, related to the existence of annular flow over a larger range of flow parameters, accompanied by an increased film thickness. Kim et al. (2001) showed that, for counter-current two-phase flow in a coiled pipe, the flow pattern transition lines moved to lower gas flow velocities. This was confirmed by e.g. Ansari and Arzandi (2012) for horizontal channels with ribs. Recently, new attention was given to two-phase flows in corrugated pipes in the framework of the mitigation of flow-induced vibrations in these pipes (Belfroid et al., 2013; van Eckeveld et al., 2017). The presence of liquid was found to reduce, and eventually mitigate, flow-induced noise. In this application, it is important to determine the minimum liquid loading required to prevent vibrations to occur, which is strongly influenced by the flow regime.

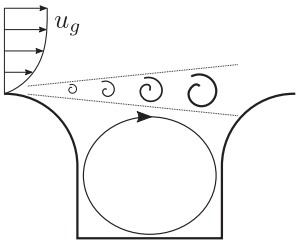

Fig. 2. Typical cavity flow in a corrugated pipe, subject to dry gas flow. The incoming gas flow separates at the upstream cavity edge, forming a shear layer where vortical structures can appear. The shear layer separates the bulk flow inside the main pipe from the recirculating flow in the cavities.

There is very limited knowledge about the effect of wall roughness on two-phase flow behavior in the annular regime. The present work aims at understanding the effect of axisymmetric ribs along a pipe wall on the flow pattern in vertical co-current two phase flow. In dry gas flow through these pipes, the quasi-stagnant flow inside the corrugations is separated from the flow through the core of the pipe. A recirculation cell is formed inside the cavities, which scales with the cavity size. There is a large variety of cavities, classified based on their geometry and internal flow structure. The geometries studied in this work are so-called shallow open cavities, where the shear layer extends to the downstream end of the cavity, and a single recirculation zone is formed inside the cavity. This regime occurs when the ratio of the length over depth ratio of the cavity is $\lesssim 8$. The specific threshold value for this regime is case and flow dependent. A schematic representation of this type of flow is provided in Fig. 2.

This work adds to understanding the effect of a corrugated pipe wall on the flow behavior in the annular regime. The behavior of liquid at the pipe walls, the entrainment ratio and the resulting droplet sizes are assessed, both for smooth and corrugated pipes. Two different corrugation geometries are studied, and water and mono-ethylene glycol (MEG) are used as working liquids, with air as the gas phase. The measurements are carried out in an open flow loop, described in Section 2, together with the experimental methods. Different measurement techniques are used to investigate the flow behavior. The film thickness in smooth pipes is measured using a *planar laser-induced fluorescence* (PLIF) technique, adapted to remove the effect of total internal reflections at the gas-liquid interface. Droplet sizing is carried out using shadowgraphy and interferometry, alongside entrainment measurements. Liquid accumulation inside the cavities is also assessed using a PLIF based technique. Measurement results for the smooth and corrugated pipes are provided in Sections 3 and 4, respectively. The results are discussed in Section 5. Section 6 provides the conclusions from the present study.

2. Experimental

2.1. Experimental set-up

The measurements are carried out in an open flow loop with a vertical test section (depicted in Fig. 3). The air flow through the pipe is provided by a blower (Esam Mediojet 2V). Gas flow rates

[1] $Re_f = 4\rho_l u_f \delta/\mu_l$, with u_f the average film velocity and δ the film thickness.

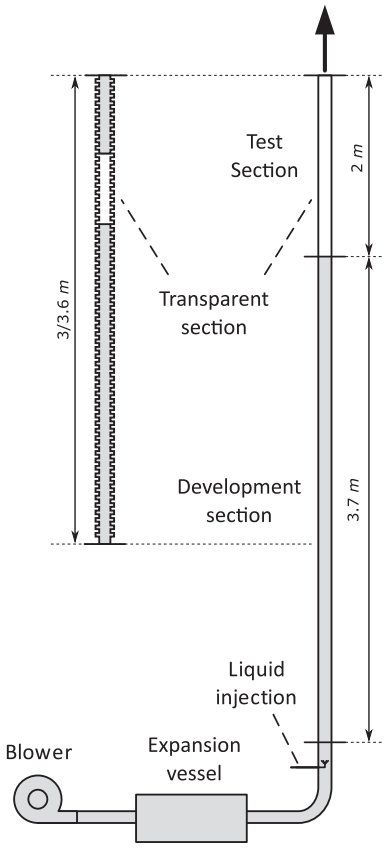

Fig. 3. Schematic representation of the experimental set-up. The gas flow is created using a blower, followed by an expansion vessel which reduces the noise amplitude from the blower. Liquid is injected with a spray nozzle at the pipe center. The test section is transparent and can be replaced by a corrugated pipe section.

are measured with a zero β-ratio, long-radius ASME flow nozzle (Leutheusser, 1964). The superficial gas and liquid velocities are used to characterize these flow rates ($u_{sg} = Q_l/A_p$ and $u_{sl} = Q_g/A_p$, with Q being the volume flow rate of the respective phase and A_p the pipe cross sectional area). After passing through the expansion vessel, the flow is directed upward and liquid is injected with spray nozzles located at the pipe center (Bete PJ8, PJ10, PJ15, PJ24 and PJ32). The various nozzles are used for different liquid flow rates. Although they produces slightly different sprays, the effect on the results is found to be negligible. A rotary vane pump (Fluid-O-Tech PA111) drives the liquid flow. The nozzles produce a dispersed spray of droplets with a nominal diameter less than 150 μm. The liquid flow rate is measured with a coriolis mass flow meter (Bronkhorst M14 CORI-FLOW). For flow development purposes, a 3.7-m long smooth pipe section ($L_p/D_p \approx 75$, with D_p being the inner pipe diameter, which is 50 mm) is placed behind the liquid injection point. It is made of steel, with a wall thickness of 5 mm. It is followed by a transparent plexiglas measurement section, which also has a wall thickness of 5 mm. The measurements are taken at approximately 84 pipe diameters downstream of the liquid injection point. The flow loop is terminated with an open outflow. Temperature measurements are performed at the outlet using a Pt100 temperature probe located at the pipe center-line. The temperature measurements, together with pressure measurements upstream of the liquid injection point, are used to correct the mass density of the gas. For the experiments with corrugated pipes, the last three meters ($L_p/D_p \approx 61$) of the flow loop are replaced with a PVC corrugated section. Due to the wide range of applications (from different heat-exchangers to industrial risers), there is a large variety in geometrical characteristics that are of

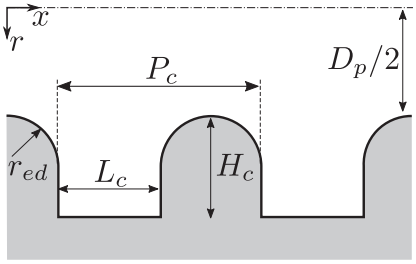

Fig. 4. Cross-section of the corrugation geometry. The symbols are explained in text and numerical values for the used geometries are given in 1.

Table 1
Dimensions of the different geometries used. Symbols are explained in the text, and a schematic of the corrugation lay-out is provided in Fig. 4.

	geom A	geom B
D_p [mm]	49.25	49.25
L_c [mm]	4	6
H_c [mm]	4	6
P_c [mm]	6	10
r_{ed} [mm]	2	2
L_p [m]	3	3.6

interest for corrugated pipe flow. For the present study, we limit ourselves to two different general corrugation geometries. Both have rectangular corrugations with a cavity height over length ratio of 1 ($H_c/L_c = 1$). The upper edges are rounded (with the edge rounding radius r_{ed}) as is found in many applications (e.g. tape-wire inserts in heat and mass transfer enhancement applications). The pitch (P_c) is limited, to fit a sufficient number of corrugations in the vertical distance in order to ensure full flow development. A schematic representation of the used geometries is depicted in Fig. 4. The dimensions are given in Table 1. For optical access a transparent corrugated section is placed just before the end of the corrugated pipe, at $49 \leq L_p/D_p \leq 53$ from the corrugated pipe entrance.

2.2. High speed imaging

To characterize the annular liquid film at the pipe wall, a combination of high speed imaging and *planar laser-induced fluorescence* (PLIF) is used. From the high speed images, the flow regime and temporal film statistics are obtained. A Photron Fastcam APX 1MP camera is used, equipped with a 105 mm Micro-Nikkor objective. The transparent section is illuminated from the back using an LED panel. A grid with alternating black and white lines is placed between the light source and the pipe to increase contrast of the gas-liquid interface in the visualization images. Images are recorded at 700 Hz, which is sufficient to capture the dynamic behavior of the film.

2.3. Film thickness measurements

The film thickness is obtained from the PLIF measurements. The method used before by e.g. Schubring et al. (2010) is adapted for this purpose, with the aim to remove large reflections at the gas-liquid interface. The set-up is schematically depicted in Fig. 5a. A laser sheet (from an Nd:YAG LitronLasers Nano L 50-50) illuminates the liquid film. The liquid contains a fluorescent dye (150 µg/L rhodamine WT). The fluorescent light is recorded using a CCD camera (LaVision Imager LX 16M), equipped with a 105 mm Micro-Nikkor objective with a red filter (B+W 62 041) in front of it. The viewing angle has been optimized in terms of wall-normal

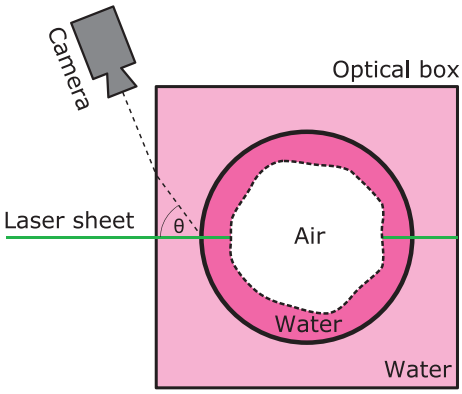

(a) Schematic of the PLIF set-up used in the film thickness measurements, seen from the top. The water at the interior of the pipe is dyed with 150 $\mu g/L$ rhodamine WT, water in the optical box with 50 $\mu g/L$.

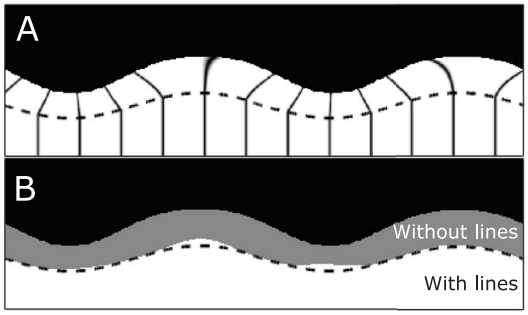

(b) Example images obtained using an inverse ray-tracing technique for θ of 75°, with (A) the image obtained by the sensor (the dashed line indicates the real interface), and (B) the results obtained with and without using the line detection method.

Fig. 5. Principles of the liquid film thickness measurements.

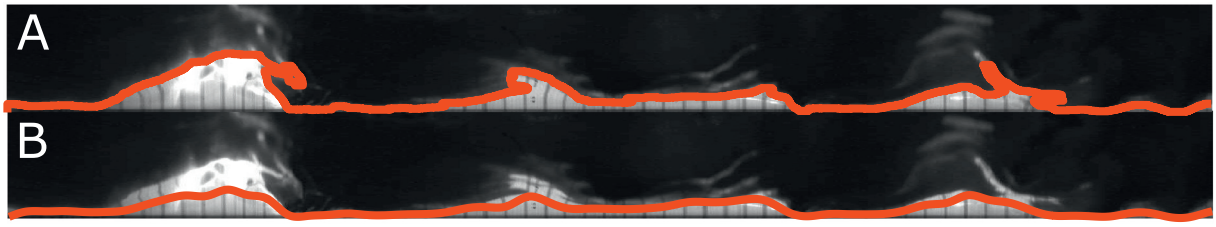

Fig. 6. Comparison of film thickness from binarization (A) and using the novel line detection method (B). Large reflections can be detected in B because of the deviation of the lines.

spatial resolution of the film and the amount of reflections observed, resulting in an angle w.r.t. the laser sheet (θ in Fig. 5a) of 75°.

A drawback of the described optical technique is the overestimation of the film thickness due to total internal reflections at the air-water interface. Häber et al. (2015) showed that the overestimation of the film thickness could reach a factor of two for steep waves. In order to reduce this error, the regular light sheet used by Schubring et al. (2010) is replaced by a *lined* light sheet. A comparable method is presented by Charogiannis et al. (2017) for downward annular pipe flow. The light sheet consists of alternating light and (smaller) dark regions, as is visible in Fig. 6. The dark lines are generated by passing the light sheet through a grid, thereby creating shadows behind the grid lines. A reflection of the light sheet at the wavy air-water interface will cause the lines to deviate from their straight path, enabling a distinction between the actual film and the reflections. A drawback of this method is the reduced spatial resolution of the film thickness measurement. The spatial resolution in the streamwise direction is now associated with the number of grid lines in the light sheet, instead of the number of pixels in that direction. No prism is used in the experiments. Since the camera is relatively far away (paraxial approximation is allowed), knowing the pipe wall thickness and the spacing of the dark lines in the light sheet is sufficient to spatially calibrate the system.

An inverse ray-tracing technique is used to validate the method. Fig. 5b shows an example image obtained with this technique for a simple sine wave. The initial position of the lines is obtained using a peak-find algorithm, with the average image as input. Deviation of the lines is detected using a run-length encoding script, determining the first wall-normal location where the lines show a 2 pixel deviation from the initial position over at least 5 pixels in wall-normal direction. For this artificial wave the improvement in film thickness measurement is evident. Only where the light rays have a (near-)perpendicular angle of incidence with respect to the gas-liquid interface, the wave height is overestimated.

This technique is applied for the film thickness measurements in a smooth pipe. Line spacing was chosen to be 1 mm, which is deemed sufficient to capture most waves, keeping in mind the capillary length scale (2.7 mm in the air-water case). Decreasing the line spacing further would complicate the line detection method. Fig. 6 shows a part of a typical image obtained from these measurements, visualizing the improvement when the line detection method is used.

2.4. Cavity filling measurements

The liquid accumulation inside the cavities of the corrugated pipe is also measured using a PLIF-based method, similar to the film thickness measurements. In this case, the reflections at the air-water interface are reduced by reducing the viewing angle with respect to the laser sheet. An angle of approximately 25° is used between the laser sheet and the camera. With a steady and perfectly axisymmetric gas-liquid interface within the corrugations, this yields a viewing angle well below the critical angle for air-water ($= 48.6°$) and air-mono-ethylene glycol ($= 44.0°$). The dye concentration is optimized for the required intensity of the emitted fluorescent light, resulting in a concentration of 125 µg/L. Furthermore, the optical box is filled with a Rhodamine solution of approximately 50 µg/L, and the fluorescent light emitted from this region is used to correct for non-uniformity in the laser sheet. A typical image obtained with water injection in a corrugated pipe

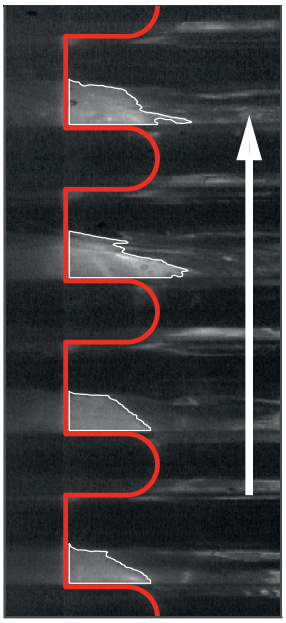

Fig. 7. Typical image of liquid accumulation in cavities for a corrugated pipe with geometry B (see Table 1). Flow is from bottom to top. The corrugated wall is marked with the red line, the white boundaries are obtained from image processing and indicate the filling regions. (For interpretation of the references to color in this figure legend, the reader is referred to the web version of this article.)

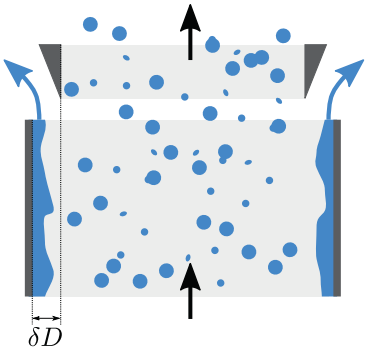

Fig. 8. Schematic representation of the slit used to remove the film from the pipe wall. δD indicates the gap width between the inner pipe wall and the slit edge, which is 2 mm at each side.

with geometry B is depicted in Fig. 7. High intensity corresponds to regions of liquid accumulation. The white boundaries are obtained after processing, and indicate the filling area. More details about the different processing steps can be found in a previous paper by van Eckeveld et al. (2017).

2.5. Film flow rate and droplet sizes

Droplet sizes are measured at the pipe end, after removal of the liquid film attached to the wall. The film is removed using a slit (as was applied by e.g. Hay et al. 1996). The slit is circular, with a wedge shaped edge. The internal diameter of the slit is 4 mm less than the internal pipe diameter. The film is collected between the slit and the inner pipe wall, and is directed to a separate container (see Fig. 8). The mass of the container is recorded over a period of at least eight minutes, to obtain the film flow rate.

Droplet size distributions are measured after film removal, with a combination of *shadowgraphic particle imaging* (SPI) and *interferometric particle imaging* (IPI, Glover et al. 1995). The techniques are combined to capture a large range of droplet sizes. A schematic overview of the SPI set-up is provided in Fig. 9. Images are acquired using a CCD camera (LaVision Imager LX 16M) equipped with a 200 mm focal length Micro-Nikkor objective. Behind the pipe, a diffuse white background is lit by a pulsed Nd:YAG laser (LitronLasers Nano L 50-50). The droplet shadows are subsequently recorded. Several image processing steps are applied. First, a background correction is applied, followed by a median filter (3x3 pixels) to reduce noise. The droplet edges are found using a canny filter and the contours are filled with a convex hull technique (Gonzalez and Woods, 2012). From the resulting binary image, the droplet sizes are obtained, assuming spherical droplets. A typical example of an SPI image obtained after background subtraction and the application of a spatial median filter is depicted in Fig. 9. The droplet size range that can be measured using this technique is limited by the spatial resolution of the images and by the optics. The spatial resolution in the reported experiments is approximately 12.5 μm/pixel. Furthermore, the diffraction limit of the imaging system is around 25 μm. It is therefore difficult to obtain reliable drop sizes for droplets with $d_p <$ 50 μm using shadowgraphy.

An interferometric technique is used to measure droplets with smaller diameters. The droplets are illuminated with a 1 mm thick laser sheet, as is schematically depicted in Fig. 10. The same camera is used for the SPI and IPI measurements. It is placed at an angle of 70° with the laser sheet, and the Scheimpflug condition is fulfilled to obtain equal focusing over the entire field of view (Adrian and Westerweel, 2011). The 70° angle results in a high signal-to-noise ratio of the interference fringes, especially when laser light with a parallel polarization is used (Damaschke et al., 2005). A separate aperture is placed just before the camera lens. Illumination of a spherical droplet with a light sheet results in two glare-points at both sides of the droplet. A defocused image of these glare points yields a disk with an interference pattern due to the monochromatic laser light that is used. A typical raw IPI image is depicted in Fig. 10. There is a direct relation between the spacing of the fringes and the droplet size. When the ratio of refractive indices of the droplets and the surrounding fluid is larger than unity ($m = \frac{n_l}{n_g} > 1$) this relation is (Damaschke et al., 2005):

$$d_p = \frac{2\lambda}{\Delta\psi}\left(\cos(\theta/2) + \frac{m\sin(\theta/2)}{\sqrt{m^2 - 2m\cos(\theta/2) + 1}}\right), \tag{1}$$

with d_p being the droplet size, λ the wavelength of the used light, $\Delta\psi$ the angular fringe spacing, and θ the viewing angle. The advantage of using an interferometric technique is that the size of the interference disks is not related to the droplet size, but rather to the optical choices made in designing the set-up. Small droplets yield a large $\Delta\psi$, and the lower bound of the droplet size that can be measured is solely determined by the aperture size and the working distance. The detection of large droplets is limited by the spatial resolution of the camera image as it corresponds to the smallest fringe spacing that can still be detected accurately. A correlation method is used to locate the droplets in the images. The entire image is correlated with a circular mask, having the size of the interference disks. Peaks in the resulting correlation plane are associated with the locations of the droplets. Overlapping parts of the droplets are removed and the fringe spacing is found from a simple periodogram, obtained using a Fast Fourier Transform of the vertically-averaged disk images. The fringe spacing is subsequently used to calculate the droplet size.

Combination of IPI and SPI

SPI and IPI recordings are carried out subsequently, assuming stationary and reproducible conditions at specific flow settings. The validity of this assumption is verified by repeating experiments on different measurement days. Fig. 11 shows droplet size distributions obtained from SPI and IPI at the same flow conditions. The

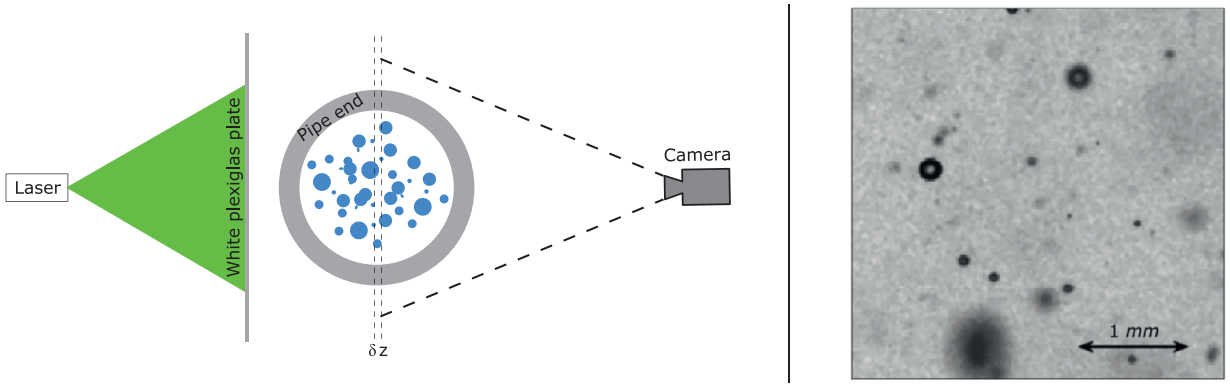

Fig. 9. Schematic representation of the shadowgraphy set-up (left), where δz depicts the depth of focus of the imaging system. A cut-out of a typical image obtained using the shadowgraphic measurement technique (right), after background subtraction and the application of a median filter. Dark spots are the shadows of droplets, used to find the droplet size.

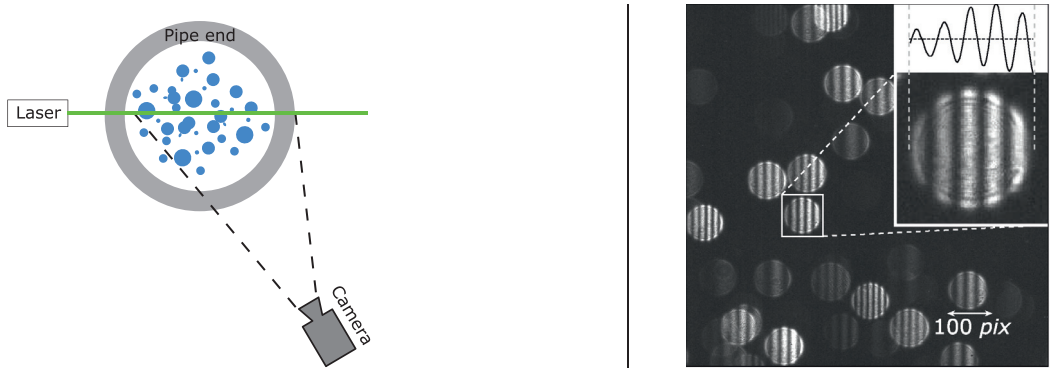

Fig. 10. Schematic representation of the IPI set-up (left) and a cut-out of a typical image obtained with this method (right). The insert shows the normalized interference pattern obtained from the enlarged droplet image after normalization and the application of a moving average filter.

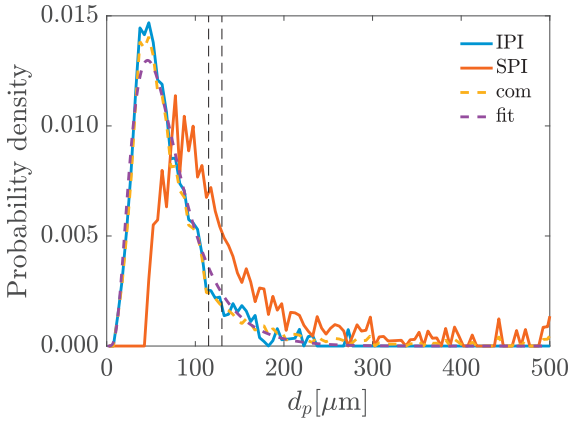

Fig. 11. Volumetric droplet size distributions obtained from IPI and SPI, and the resulting combined and fitted distribution. The vertical dashed lines indicate the combination region for this particular case.

overlapping region in droplet diameter, indicated by the dotted lines, is used to combine the two distributions into a single distribution covering the entire droplet size range observed in the experiment. The probability of a droplet ending up in the overlapping range (i.e. $a \leq d_p \leq b$) for the two techniques is:

$$P_{ipi}^{ab} = \frac{N_{ipi}[a \leq d_p \leq b]}{N_{ipi}}, \quad \text{and} \quad P_{spi}^{ab} = \frac{N_{spi}[a \leq d_p \leq b]}{N_{spi}}, \tag{2}$$

where N_{ipi} and N_{spi} are the number of droplets obtained from IPI and SPI, respectively. Since the distributions from IPI and SPI are subsets of the full droplet size distribution, it holds that $C_1 \cdot N_{ipi} = C_2 \cdot N_{spi} = N_{com}$, where $C_{1/2}$ are constants. Knowing that the probability that a droplet has a diameter between a and b in the combined distribution (P_{com}^{ab}) should match for IPI and SPI, the following conversion is obtained:

$$P_{com}^{ab} = \frac{\frac{1}{C_1}N_{ipi}[a \leq d_p \leq b]}{N_{com}} = \frac{\frac{1}{C_2}N_{spi}[a \leq d_p \leq b]}{N_{com}}. \tag{3}$$

The combined drop size distribution then becomes:

$$P_{com}N_{com} = \begin{cases} N_{ipi} & \text{if } d_p \leq b \\ \frac{C_1}{C_2}N_{spi} & \text{if } d_p > b, \end{cases} \quad \text{with } \frac{C_1}{C_2} = \frac{N_{ipi}[a \leq d_p \leq b]}{N_{spi}[a \leq d_p \leq b]}. \tag{4}$$

The result of this operation for one particular case is shown in Fig. 11. The figure also shows the fitted upper limit log normal (ULLN) distribution, as was also used by e.g. Azzopardi (1997) to describe the droplet size distribution in annular smooth pipe flow. This distribution is fitted to the combined volumetric droplet size distribution and statistical measures regarding the droplets are obtained from the fit.

3. Two-phase flow in smooth pipes

As a reference for the corrugated pipe flow, two-phase flow in a smooth pipe is first assessed. To the knowledge of the authors there is no literature data available for the very low liquid loading used in the presented experiments, and which is relevant in various applications. The liquid volume fraction attained in the experiments is $\phi_l < 2 \times 10^{-4}$. This operating range is particularly relevant for corrugated risers (Belfroid et al., 2013). Furthermore, at

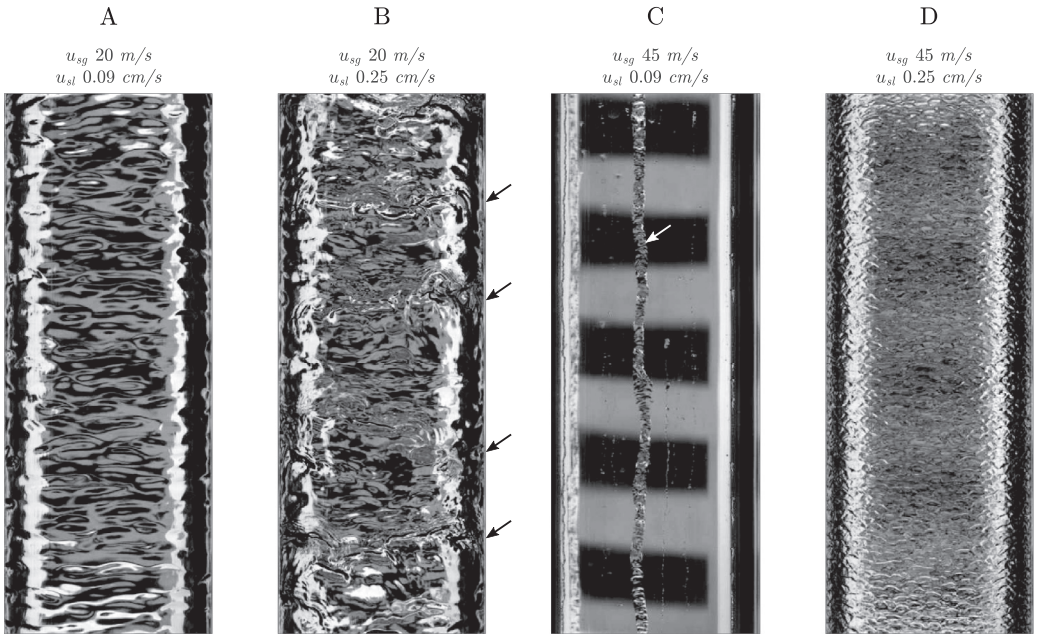

Fig. 12. Different film flow regimes observed from the high speed video recordings. (A/D) ripples, (B) ripples and disturbance waves, (C) rivulets. The superficial gas and liquid velocities are indicated on top, in m/s and cm/s, respectively. The black and white bands in the background are used to increase the contrast in the film shadowgraphs. The black arrows indicate the position of disturbance waves in B, whereas the white arrow shows the rivulet observed in C.

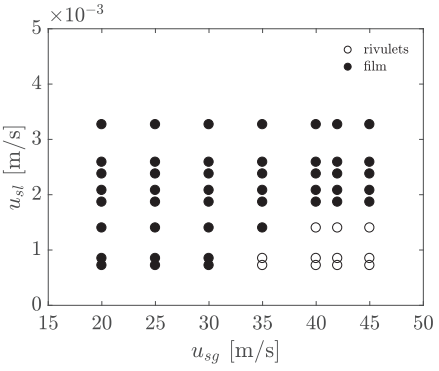

Fig. 13. Flow map for the experimental parameter space, indicating the regions where a full film and rivulets occur in the smooth pipe.

the onset of condensation in heat exchangers or in dry-out conditions, mass fractions in this range will also occur. The present results are compared to data obtained by Belt et al. (2010) and to the data presented in the review paper by Azzopardi (1997), which are both for a higher liquid loading.

The high speed video recordings of the liquid film reveal three different flow patterns: rivulets, regular ripples and disturbance waves. Fig. 12 shows snapshots of the different flow regimes. Full high-speed recordings are added as supplementary material to this paper, and can be found online. For low liquid loading at high gas flow rates the film is not sustained and dry spots appear. This results in the formation of rivulets, transporting all the liquid that is attached to the wall (C in Fig. 12, supplementary recording 'R3'). The width of the rivulets varies from approximately 0.5 to 5.0 mm. The region where rivulets are observed in the data is depicted in Fig. 13. For most of the parameter space in this study, the film is only covered with ripple waves (A and D in Fig. 12, supplementary recordings 'R1' and 'R4', respectively) which are smaller regular waves, with a limited azimuthal coherence. For high liquid loading at low gas flow velocity, disturbance waves start to appear (B in Fig. 12, supplementary recording 'R2'). These waves have a significantly larger amplitude than the ripples and travel at a higher velocity. They also show a strong coherence along the circumference of the pipe.

The occurrence of disturbance waves becomes very clear from the time-space diagrams, obtained using the high speed images. These diagrams are obtained from the centerline of the pipe images, in streamwise direction. Figs. 14a and c show cases where only ripples are present. Increasing the liquid loading for the same gas flow rate results in the onset of disturbance waves on top of the ripples (Fig. 14b). They are observed as steep bands with smaller waves. From the slope of these bands the wave speed can be obtained. For the disturbance waves in Fig. 14b this is approximately 0.45 m/s, whereas the ripples in Fig. 14a travel at a significantly lower velocity (around 0.06 m/s). The difference in wave speed is caused by the increased penetration depth of the disturbance waves into the interfacial gas boundary layer. The wave speed is compared to the correlation proposed by Kumar et al. (2002) and more recently revisited by Sawant et al. (2008). This correlation results in an over-prediction of the wave speed by a factor 1.7. It is, however, not validated below the onset limit of disturbance waves. Furthermore, Sawant et al. (2008) report that the wave speed is dependent on the pipe diameter, which is smaller than in the current experiments.

From literature it is expected that disturbance waves would not occur in the reported experiments, although a large scatter of the experimental data around the onset boundary of disturbance waves has been observed (Azzopardi, 1997; Sawant et al., 2009). The axial distribution of the disturbance waves observed in the high-speed video recordings is highly irregular, indicating operation close to the onset of the waves. Decreasing the liquid loading results in their disappearance, in accordance with the onset boundary found by e.g Sawant et al. (2009). They report that an increase in the superficial gas velocity results in a higher liquid loading required for disturbance waves to occur, which is also observed in our experiments. From the PLIF data it is difficult to distinguish disturbance waves from other waves. Temporal information (wave speed) is required to separate these waves from other high-amplitude bursts (Belt, 2007).

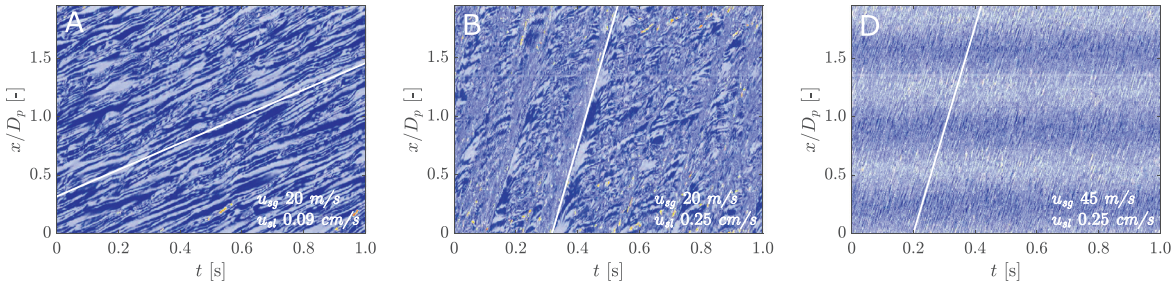

Fig. 14. Time-space diagrams of the image intensity along the pipe centerline for u_{sg} = 20 (a,b) and 45 m/s (c), and u_{sl} = 0.09 (a) and 0.25 cm/s (b,c). The white lines indicate the wave speed of the ripple (a,c) and disturbance (b) waves. The letters in the top left corners correspond to the letters used in Fig. 12.

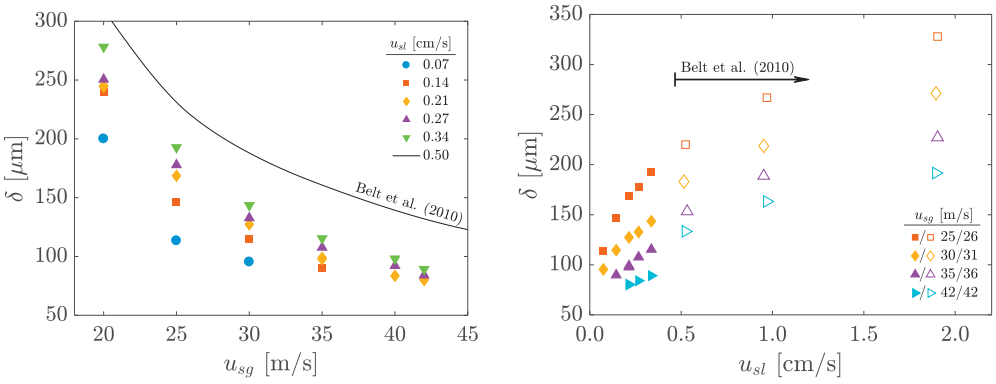

Fig. 15. Film thickness (δ) as a function of (a) superficial gas velocity and (b) superficial liquid velocity. The solid line in (a) and open symbols in (b) are experimental data by Belt et al. (2010).

The instantaneous film thickness (δ) can be obtained from the PLIF measurements. Figs. 15a and b show the average film thickness with respect to the superficial gas velocity and superficial liquid velocity, respectively. A strong reduction in δ with an increasing gas velocity is observed, which is related to the increased film flow velocity. Although no experimental data is available for the low liquid loading used in the present measurements, the results obtained by e.g. Belt et al. (2010), which are also included in Fig. 15a, show the same trend. The effect of the liquid loading on δ is also significant, but considerably lower than that of the gas velocity. The standard deviation of the film thickness, which is a measure for the interfacial wave height, shows similar trends with u_{sg} and u_{sl} as the film thickness. Plotting it as a function of the film thickness itself makes all data collapse onto a single straight line, indicating the linear dependence of the wave height on the film thickness, as is also found in literature (Belt et al. 2010, see Fig. 16).

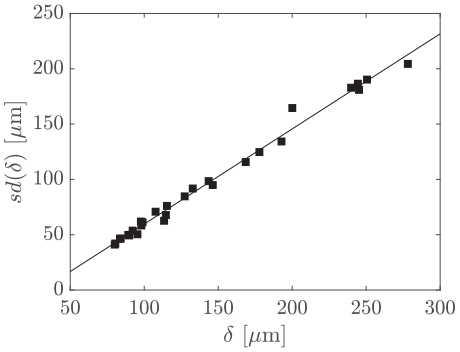

Fig. 16. Standard deviation of film thickness as a function of the film thickness. The solid line corresponds to a linear fit of all data (with a slope of 0.86).

At the current operating conditions, low liquid entrainment is expected. The absence of disturbance waves in the largest part of the measurement domain corroborates this expectation. Quantitative measures for the amount of entrainment are obtained from film flow rate measurements, as described in Section 2.5. The entrainment ratio is defined as $E = \frac{Q_{tot} - Q_{film}}{Q_{tot}}$, in which Q denotes the respective liquid flow rate. The entrainment ratio as a function of the gas flow rate is depicted in Fig. 17a. An expected increase with the superficial gas flow velocity is observed, originating from the increase of entraining shear forces at the gas-liquid interface. The entrained liquid fraction seems to decrease with increasing liquid loading; the entrainment measurements are, however, somewhat compromised by the evaporation of liquid into the gas flow, effectively changing the total liquid flow rate through the smooth pipe. The actual liquid loading in the measurement section is therefore lower than the liquid loading at the injection point. The evaporation rate is estimated using the corresponding Sherwood number for mass transport in internal pipe flow: $Sh = 0.023 Re_g^{0.83} Sc^{0.44}$ (Gilliland and Sherwood, 1934), where $Sc = \mu_g / \rho_g D_p$ is the Schmidt number. The mass transfer rate is subsequently calculated according to: $\dot{n}_w = k_c A_f \frac{(p_w - p_w^{sat})}{RT}$, where k_c is the mass transfer coefficient ($k_c = ShD_v/L_p$), A_f the interfacial area, p_w the partial pressure of water and R and T the ideal gas constant and the temperature, respectively. Depending on the atmospheric humidity, the liquid flow rate could be corrected using this expression. Unfortunately, no humidity measurements were carried out during the measurements, hence an accurate estimation of the evaporation rate could not be obtained. Using daily meteorological humidity data, an estimate of the evaporation rate is obtained, and

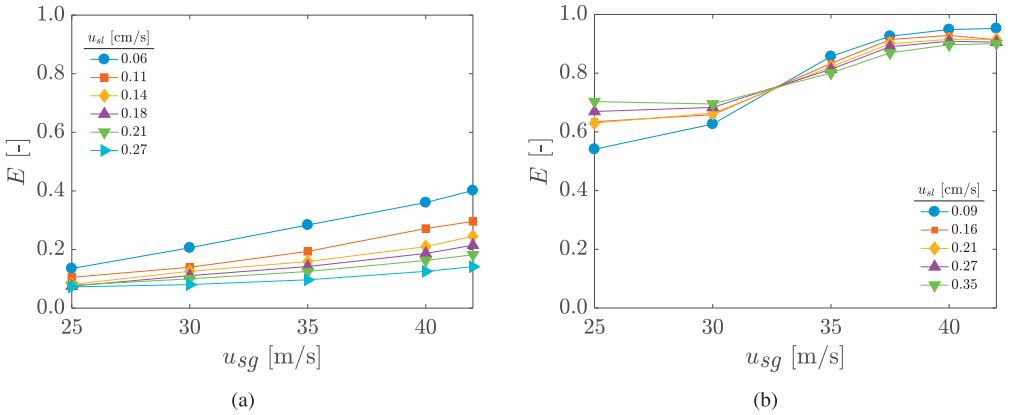

Fig. 17. Liquid entrainment ratio as a function of the superficial gas velocity u_{sg} for different values of the superficial liquid velocity u_{sl}, in smooth (a) and corrugated pipes(b, geom A).

is found to be in the same order as the entrainment rate observed in Fig. 17a. As expected, the actual entrainment will therefore be close to zero. The exact entrainment ratio is, however, not the main purpose of the present study. A qualitative analysis of the effect of corrugations on the entrainment ratio can be performed based on the reported measurements.

4. Two-phase flow in corrugated pipes

With the smooth pipe case as a reference, the flow behavior in corrugated pipes is now described. This is done for the corrugation geometries presented in Section 2, and for superficial gas and liquid velocities as used in the smooth pipe experiments. As a consequence of the presence of corrugations, the flow regime changes significantly. It is impossible to make the same distinction between a full film and rivulets, as is done for the smooth pipe. Measurements of the liquid entrainment, droplet sizes and the liquid accumulation inside the cavities, however, can provide physical insight in the two-phase flow behavior in corrugated pipes.

4.1. Entrainment

The entrainment ratio measured for the corrugated pipe with geometry A is depicted in Fig. 17b. For higher gas flow rates, almost all liquid is transported as droplets in the gas core of the flow. Evaporation in this pipe is expected to be limited: the large entrainment ratio results in a very short residence time of liquid in the pipe, compared to the smooth pipe. Reducing the superficial gas flow velocity from 42 to 25 m/s causes a strong reduction in the amount of liquid entrainment. The entrainment ratio decreases from around 0.95 to 0.6. A critical point occurs for a gas velocity between 30 and 35 m/s, where a step in the entrainment is observed. The effect of the liquid flow rate is relatively limited compared to the effect of the gas flow rate. However, the trend in the liquid entrainment before and after the 'step' is opposite. At lower gas flow rates, the lowest entrainment is observed for the lowest liquid flow rate. For $u_{sg} \geq 35$ m/s, this trend is reversed. Furthermore, liquid entrainment into the gas core is in all cases considerably higher in the corrugated pipe as compared to the smooth pipe (compare Fig. 17a and b).

4.2. Droplets in the core

For most of the parameter range, the majority of liquid is transported as droplets in the gas core of the pipe flow. The droplet size distributions obtained from SPI and IPI are combined by matching them around $d_p = 80$ µm, to obtain a single distribution (see Section 2.5 for details on the combination of SPI and IPI). Droplet sizing is carried out for a subset of the parameter range, to observe general trends. Fig. 18a gives a typical volumetric droplet size distribution (at $u_{sg} = 35$ m/s and $u_{sl} = 0.07$ cm/s). The dashed line shows the fitted ULLN distribution for this case. The Sauter mean diameter ($d_{32} = 6\ V_p/A_p$, with V_p and A_p being the droplet volume and its diameter, respectively) is obtained from the fit, to quantitatively compare the distributions for different flow settings (see Fig. 18b). The superficial liquid velocity does not affect the droplet size significantly. There is however a strong decrease in droplet size with increasing gas flow rate. Similar trends have been observed for droplets in smooth pipe flow caused by the increased shearing forces exerted on the generated droplets. Droplets observed in the corrugated pipe are significantly larger than expected for a smooth pipe (approximately 30%). Entrainment from corrugations results in larger fragments of liquid being introduced to the gas core, due to the locally increased film thickness inside the cavities. This higher film thickness causes larger fragments to be entrained into the gas flow. The small pitch length of the investigated geometries results in the presence of larger fragments throughout the entire gas core.

4.3. Cavity filling

Due to the corrugations and the short pitch length, a continuous liquid film is not formed for most of the parameter space. Liquid accumulates in the cavities between the corrugations. This liquid accumulation is measured using a PLIF technique (as explained in Section 2). The fraction of the cavity volume occupied by liquid (indicated with α) has been used to quantify the amount of liquid in the cavities. α is obtained from the temporal- and spatial-averaged data over all cavities in the field of view. The resulting filling is strongly dependent on the gas flow rate, as is depicted in Fig. 19a. For $u_{sg} < 30$ m/s, the cavities are entirely filled up. There is a liquid film at the wall, skipping over the cavities, essentially reducing the wall roughness experienced by the gas flow. For higher values of u_{sg}, a linear reduction in α is observed. This reduction is mainly manifested at the downstream cavity side. Liquid is removed from the downstream side by the augmented shearing forces exerted by the gas flow. The remaining liquid inside the cavities is dragged towards the upstream cavity edge by the mutual action of gravity and the internal cavity flow. Liquid is re-entrained into the gas core of the flow by the shearing recirculating gas flow above the interface. The effect of the liquid loading is depicted in Fig. 19(b). The filling is plotted against the liquid volume fraction ($\phi_l = Q_l/Q_{l+g}$) to facilitate the comparison for different superficial gas velocities. Filling of the cavities increases with the liquid flow

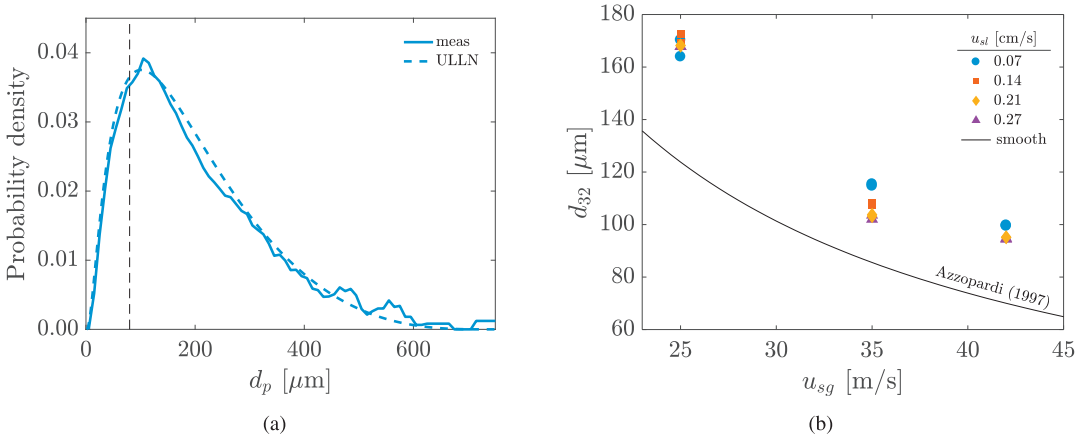

Fig. 18. (a) Example of a combined droplet size distribution in the corrugated pipe (geometry A) for $u_{sg} = 35$ m/s and $u_{sl} = 0.07$ cm/s, the dashed vertical line indicates the center of the SPI-IPI merging region. (b) Sauter mean diameter of the combined droplet size distributions in a corrugated pipe (geometry A) as a function of superficial gas flow speed. The solid line indicates a correlation for the droplet size in smooth pipes (Azzopardi, 1997).

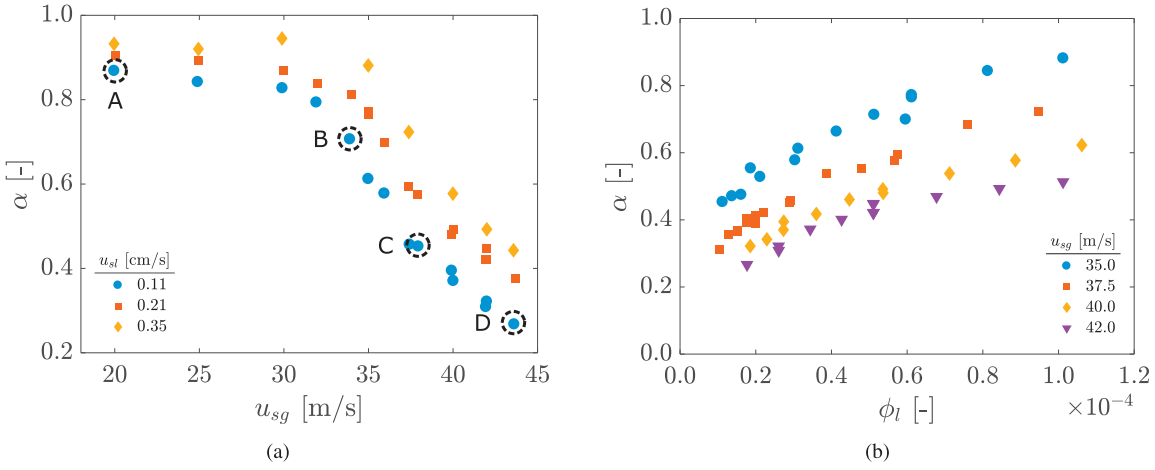

Fig. 19. Cavity filling as a function of the superficial gas speed u_{sg} (a) and the liquid volume fraction ϕ_l (b). A–D in (a) correspond to the respective filling contours displayed in Fig. 20.

rate, due to the larger liquid influx into the cavities. Typical filling profiles, illustrating the different stages of the liquid filling, are depicted in Fig. 20.

As shown in Fig. 17(b), there is significant entrainment in the corrugated pipe. Entrained liquid in the core of the pipe is expected to be spatially isolated from the cavities at the outer radius of the pipe. Mainly liquid transported close to the pipe wall interacts with the internal cavity flow, affecting the liquid cavity filling. Therefore, the liquid entrainment ratio, averaged for different liquid flow rates, is used to correct the superficial liquid velocity. This results in a superficial liquid film velocity (defined as $u_{sf} = (1 - E)u_{sl}$). Plotting the filling α as a function of this u_{sf} causes the data for the various gas flow rates to collapse onto a single line (see Fig. 21). This indicates that the effect of the gas flow rate on the filling is mainly caused by an increase in entrainment for increasing u_{sg}. It, therefore, implies that the entrained liquid does not interact with the internal cavity flow and hence, does not result in additional liquid being trapped in the cavities.

4.4. Cavity geometry and liquid properties

To assess the effect of cavity size and properties of the injected liquid on the two-phase flow behavior, additional experiments are carried out using a corrugated pipe with geometry B (see Table 1) and/or with mono-ethylene glycol (MEG) as working liquid. Geometry B is similar to geometry A, but the cavity depth and length are enlarged by 50%. MEG is approximately 19 times more viscous than water at atmospheric conditions, whereas the surface tension is significantly reduced (from 72 mN/m for water to 48 mN/m for MEG, see Lide, 1994). Attempts were made to use aqueous glycerol solutions to keep the surface tension change limited. However, water evaporation from the solution caused the liquid properties to change over the length of the pipe, troubling the results.

For the corrugated pipe with geometry B, the entrainment ratio approaches one, irrespective of the gas flow rate and liquid loading (Fig. 22(b)). The step in the entrainment ratio, observed for geometry A, does not occur for geometry B, within the current parameter space. This is related to the filling fraction α, which never attains values above 0.6 for this geometry, even for lower gas flow rates (as is depicted in Fig. 23(b)). The filling shows the same steady increase with increasing liquid loading, but the upper limit is never reached, and it probably occurs at a higher liquid loading. It was shown for geometry A, that at total cavity filling ($\alpha \to 1$) the entrainment significantly reduces. For lower filling ratios, nearly full entrainment is exhibited ($E \to 1$). Similar principles hold when injecting MEG instead of water (Figs. 22(a) and 23(a)). The absolute values of the entrainment ratio for MEG are slightly lower compared to water, for both corrugation geometries. Also the filling ratio is lower. The trends in both filling and entrainment are similar for water and MEG. The large increase in viscosity when switching

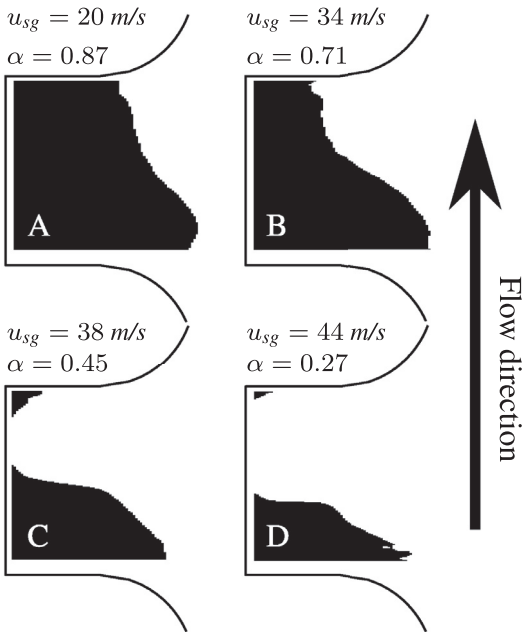

Fig. 20. Liquid cavity filling profile, measured with the PLIF method described in Section 2, for the four different cases indicated in Fig. 19a. Flow is from bottom to top and dark regions are regions of liquid accumulation, for $u_{sl} = 0.11$ cm/s.

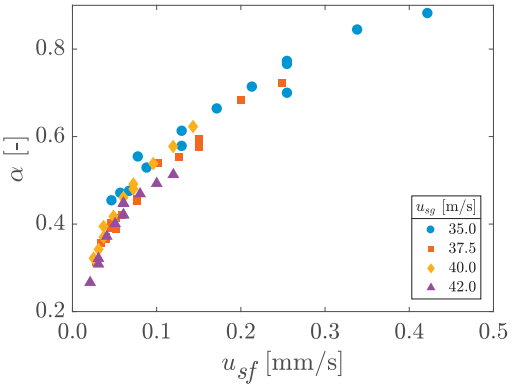

Fig. 21. Liquid filling fraction α as a function of the superficial liquid film velocity (u_{sf}) for different values of superficial gas velocity (u_{sg}).

from water to MEG does not have a strong effect on either filling or entrainment.

5. Discussion

The entrainment of liquid in two-phase corrugated pipe flow is strongly related to the cavity filling. The liquid entrainment ratio E sharply increases when liquid is removed from the individual corrugations. The recirculating gas flow inside the cavities drags liquid back into the gas core (as depicted in Fig. 24). It is assumed that this process is governed by shearing-off of waves at the gas liquid interface inside the cavities. Due to the relatively high gas flow velocity and the locally increased film thickness as a consequence of the presence of the cavities, it is safe to assume that indeed the ligament break-up mechanism (see Fig. 1) is dominant. There is a balance between drag force, exerted by the shearing gas flow, and the retaining force due to surface tension. Whenever the drag force on the interfacial wave crests exceeds the retaining force ($F_d \geq F_\sigma$), liquid packets are removed from the interface and entrained in the gas flow. The drag force is given by: $F_d = C_d \lambda h_w \rho_g u_w^2/2$, with the drag coefficient C_d, the wavelength λ, the wave height h_w and the relative velocity difference between the liquid and gas flow u_w. The retaining surface tension force is given by $F_\sigma = C_s \lambda \sigma$, with C_s depending on the wave shape. Using this force balance as a starting point, Ishii and Grolmes (1975) derived the following entrainment criterion:

$$\frac{\mu_l u_g}{\sigma}\sqrt{\frac{\rho_g}{\rho_l}} \geq 11.78 N_\mu^{0.8} Re_l^{-1.3}, \tag{5}$$

where N_μ is the viscosity number, which will be defined in Eq. 6. In a later study, Ishii and Mishima (1989) derived a correlation for the entrained fraction of liquid, based on the previously postulated onset criterion. Assuming that all excess liquid (above the critical entrainment limit from Eq. (5)) is actually entrained, they found that the entrainment ratio E is a function of the liquid Reynolds number and the Weber number ($E = f(We^{1.25} Re_l^{0.25})$). The Weber number ($We = \frac{\rho_g u_c^2 L}{\sigma}$) indicates the balance between the retaining forces (surface tension) and disturbing forces (shear at the gas/liquid interface). The cavity recirculation velocity is defines as $u_c = u_{sg}/4$, which is representative for a cavity flow (Koschatzky et al., 2011). The liquid Reynolds number ($Re_l = \frac{\rho_l u_{sl} L}{\mu_l}$) is a measure for the effect of the viscous forces inside the liquid. The critical Re_l for annular gas-liquid flow is not reached in most of the current experiments, due to the very low liquid loading. Therefore,

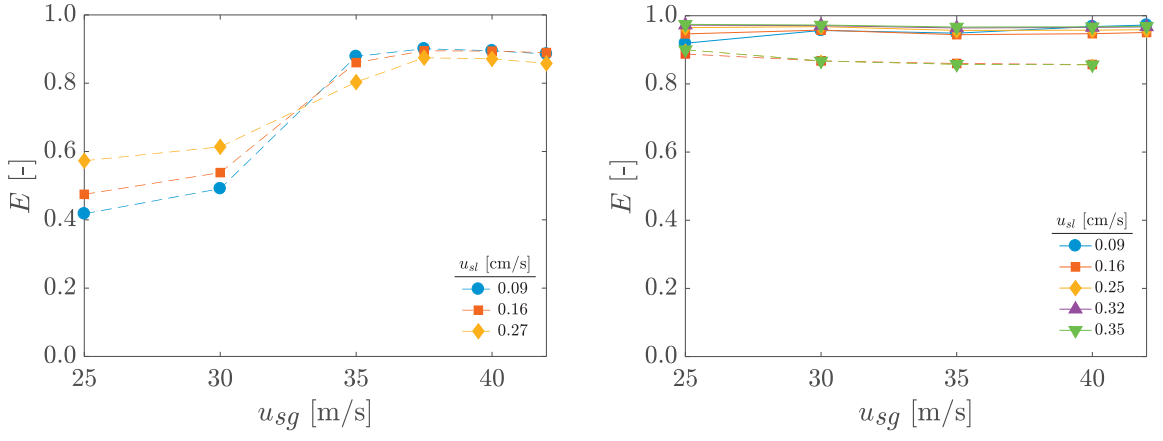

Fig. 22. Liquid entrainment as a function of the superficial gas velocity in a corrugated pipe, for different liquid loadings. Pipe with geometry A (a) and geometry B (b). Solid lines are for water, dashed lines for MEG. Results for water injection in geometry A are depicted in Fig. 17(b).

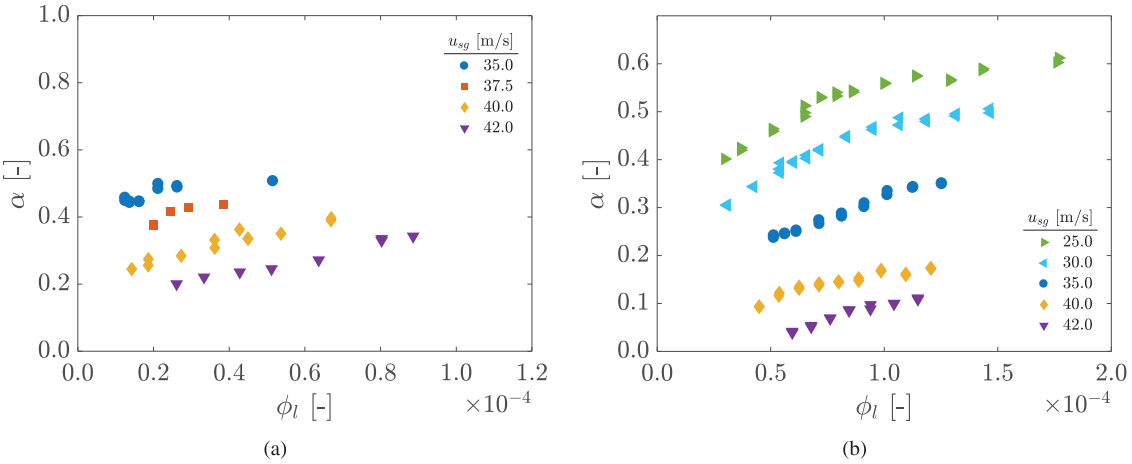

Fig. 23. Cavity filling as a function of liquid volume fraction ϕ_l, for different superficial gas flow speeds. (a) Filling for MEG injection in geometry A, and (b) for water injection in geometry B.

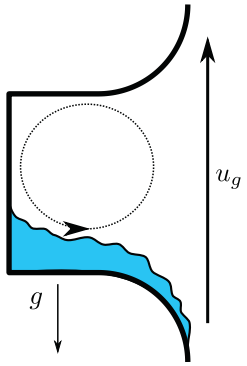

Fig. 24. Schematic of the internal cavity flow, removing liquid from within the corrugation.

the entrainment in the smooth pipe flow is very low (see Fig. 17a). This is caused by the thin liquid film, entirely submerged in the interfacial gas boundary layer (Ishii and Grolmes, 1975). The cavities in the corrugated pipe, however, cause local liquid accumulation, resulting in a significantly increased film thickness from which entrainment will occur. The dependency on Re_l is therefore different in corrugated pipe flow. In smooth pipes, the entrainment is positively correlated to the liquid Reynolds number. In corrugated pipes, however, entrainment is related to liquid accumulation in the cavities. A larger liquid Reynolds number (indicating more liquid being transported) leads to an increase in cavity filling, which reduces the entrainment. To arrive at Eq. (5), it was assumed that $N_\mu^{0.8} \approx 3N_\mu$. The viscosity number N_μ is a fluid property, and is defined as:

$$N_\mu = \frac{\mu_l}{\left(\rho_l \sigma \sqrt{\frac{\sigma}{g(\rho_l - \rho_g)}}\right)^{1/2}}. \tag{6}$$

The assumption holds for low viscosity liquids, typically when $N_\mu < 0.01$. For MEG, used in the present study, it is not valid, and $N_\mu^{0.8}$ is used instead of $3N_\mu$. Assuming that the gas-filled part of the cavity volume $(1-\alpha)$ is related to the amount of liquid entrainment from the cavity, it can be approximated by:

$$(1-\alpha) = f(We^{1.25} Re_l^n). \tag{7}$$

The relevant length scales for the Weber and Reynolds number are associated with the cavity filling. The length scale in the definition of We is taken as half the empty cavity size ($L = 1/2(1-\alpha)L_c$), whereas for Re_l, it is taken as $L = \alpha L_c$. Applying these definitions to the data acquired in the reported experiments, $n = -0.25$ gives the best collapse of all data points (as presented in Fig. 25a). There is still some scatter of the data observed in the figure. As was mentioned before, instead of scaling with the total liquid flow rate, a better agreement is found by using the superficial film velocity u_{sf}. Fig. 25b shows the filling as a function of We and Re_f ($= \frac{\rho_l u_{sf} L}{\mu_l}$). It should be noted that the liquid viscosity has no effect on the filling, when this scaling is applied. This is also found in the present work. The behavior of the liquid film is completely dominated by surface tension and the shearing gas force. According to Ishii and Grolmes (1975), this holds in the low viscosity number regime (where $N_\mu \leq \frac{1}{15}$).

In the low liquid filling regime, entrainment from within the corrugations augments the total entrainment ratio. Apart from liquid entrainment originating from within the cavities, a second entrainment mechanism seems to occur simultaneously. From the entrainment measurements for geometry A (depicted in Fig. 17b) it appears that even for entirely liquid-filled cavities (at the lower u_{sg} range), around 60% of the total liquid flow rate is entrained. This can not be caused by the previously described entrainment from within the cavity. It is expected that the corrugations decrease the stability of the film and increase its wavy structure. The standard entrainment mechanisms then will be activated, where entrainment is again a function of the liquid Reynolds number and the Weber number: $E = f\left(We^{1.25} Re_l^{0.25}\right)$, as was found by Ishii and Mishima (1989). The typical entrainment ratio for water exceeds that for MEG under the same conditions. Due to the significantly higher viscosity for MEG, compared to water, the liquid Reynolds number decreases and hence, the entrainment is expected to decrease. The lower liquid Reynolds number indicates a lower film thickness at the same flow conditions, penetrating less far into the interfacial gas boundary layer. The shearing gas velocity at the interface is lower, hence the entraining forces decrease, leading to a lower entrainment ratio. For the lower filling cases, entrainment from within the cavities and from the separating ribs will co-exist. However, the interplay of these two entrainment mechanisms is still unclear.

All reported experiments are conducted in upward vertical flow direction. It is anticipated that the direction of gravity will have a strong effect on the obtained results. In a previous study, van Eckeveld et al. (2017) found that the flow direction with respect to the gravity has significant consequences for the liquid cavity filling behavior. The liquid filling ratio is considerably higher for downward

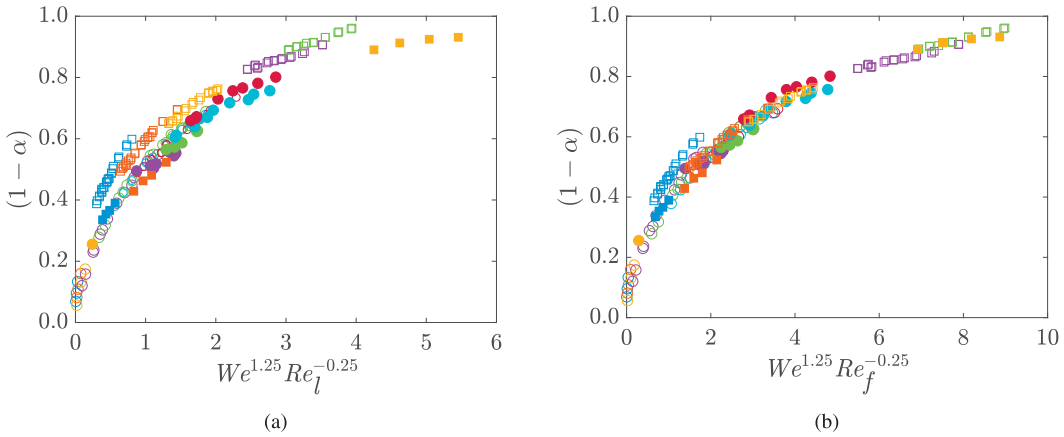

Fig. 25. Gas-filled part of the cavity $(1-\alpha)$ as a function of the Weber number and the Reynolds number based on the total liquid flow rate (a) and the film flow rate (b).

directed flow. Assuming a similar relation between cavity filling and entrainment to hold in downward flows, the liquid entrainment is expected to be reduced (see Figs. 17b and 19a).

6. Conclusions

Two-phase flow experiments are carried out in a smooth pipe and in corrugated pipes to assess the effect of the presence of corrugations on the liquid distribution in the vertical pipe flow. Film thickness measurements are performed using a novel implementation of *planar laser-induced fluorescence*. Shadows are added to the incoming laser sheet, where they appear as dark lines. The deviation of these lines at the gas-liquid interface is used to identify and remove large reflections in the PLIF measurements. Gas and liquid phase Reynolds numbers (based on the pipe diameter) are $Re_g = O(10^5)$ and $Re_l < 250$. At these conditions, liquid entrainment is not expected to be significant in smooth pipes. The entrainment ratio (corrected for evaporation) is close to zero. Furthermore, only for a very limited range of flow parameters, the onset of disturbance waves is observed, which are the main source of liquid entrainment. The film thickness is in the order of 100 μm, and the observed trends with the changing superficial gas and liquid velocities are confirmed by other experiments (with higher liquid loading), reported in literature. For very low superficial liquid velocities at high superficial gas velocities the annular film breaks up and liquid is transported as rivulets along the pipe wall.

Two-phase flow in corrugated pipes shows a very different behavior compared to smooth pipes, at the same flow conditions. Droplet sizing in the corrugated pipe reveals that considerably larger liquid fragments are transported in the gas core of the pipe, compared to the expected droplet distribution in smooth pipes. This is most likely caused by the locally (at the location of the cavities) increased film thickness, resulting in larger entrained fragments. An upper limit log normal distribution is used to describe the droplet size distribution. The liquid entrainment ratio is significantly higher in corrugated pipes than in smooth pipes. Liquid is found to accumulate in the axisymmetric cavities along the pipe wall, and the entrainment strongly correlates with the liquid-filling ratio (α). A sharp increase in the liquid entrainment ratio is observed when the filling is decreased; for totally liquid-filled cavities the entrainment is significantly lower than for partially filled cavities. This shows that the internal gas flow inside the cavity causes additional entrainment. The cavity filling α is therefore an important parameter when it comes to entrainment in these corrugated pipes. It is found to scale with the Weber and liquid Reynolds number, based on the film flow rate: the gas filled cavity volume $(1-\alpha)$ scales with $We^{1.25}Re_f^{-0.25}$. The scaling with the Weber number is similar to the scaling for entrainment in smooth pipes. The liquid Reynolds number scaling, however, is opposite. An increase in Re_f in smooth pipes leads to an increased entrainment. For partially filled cavities in corrugated pipes the filling ratio and hence the entrainment decreases with increasing Re_f.

It is shown in this work that the liquid entrainment ratio in corrugated pipes is strongly dependent on the amount of liquid accumulating in the cavities of a corrugated pipe. Future work should assess this relation for a broader range of corrugation geometries and further investigate the influence of the direction of gravity on the obtained results.

Acknowledgments

This work is funded by Shell, for which they are gratefully acknowledged. The authors thank R.W.A.M. Henkes for his valuable remarks, and E.F.J. Overmars and J. Ruijgrok for their practical help in the design of the measurements and the experimental setup.

Supplementary material

Supplementary material associated with this article can be found, in the online version, at doi:10.1016/j.ijmultiphaseflow.2018.07.004.

References

Adrian, R.J., Westerweel, J., 2011. Particle Image Velocimetry. Cambridge University Press.
Agarwal, S.K., Rao, M.R., 1996. Heat transfer augmentation for the flow of a viscous liquid in circular tubes using twisted tape inserts. Int. J. Heat Mass Transf. 39 (17), 3547–3557.
Ansari, M.R., Arzandi, B., 2012. Two-phase gas–liquid flow regimes for smooth and ribbed rectangular ducts. Int. J. Multiph. Flow 38 (1), 118–125.
Arnold, C.R., Hewitt, G.F., 1967. Further developments in the photography of two-phase gas-liquid flow. J. Photograph. Sci. 15 (3), 97–114.
Azzopardi, B.J., 1997. Drops in annular two-phase flow. Int. J. Multiph. Flow 23, 1–53.
Azzopardi, B.J., Whalley, P.B., 1980. Artificial waves in annular two-phase flow. In: Proceedings of the Basic Mechanisms in Two-Phase Flow and Heat-Transfer, ASME, pp. 1–8.
Belfroid, S.P.C., Golliard, J., Vijlbrief, O., 2013. Singing mitigation in corrugated tubes with liquid injection. In: Proceedings of the ASME 2013 Pressure Vessels and Piping Conference. American Society of Mechanical Engineers.
Belt, R.J., 2007. On the liquid film in inclined annular flow Delft University of Technology..
Belt, R.J., vant Westende, J.M.C., Prasser, H.M., Portela, L.M., 2010. Time and spatially resolved measurements of interfacial waves in vertical annular flow. Int. J. Multiph. Flow 36 (7), 570–587.

Charogiannis A., An J.S., Markides C.N., 2017. A novel optical technique for accurate planar measurements of film-thickness and velocity in annular flows. In 13th International Conference on Heat Transfer, Fluid Mechanics and Thermodynamics

Cousins, L.B., Hewitt, G.F., 1968. Liquid phase mass transfer in annular two-phase flow: droplet deposition and liquid entrainment. Technical Report. AERE.

Damaschke, N., Nobach, H., Nonn, T.I., Semidetnov, N., Tropea, C., 2005. Multi-dimensional particle sizing techniques. Exp. Fluids 39 (2), 336–350.

van Eckeveld, A.C., Westerweel, J., Poelma, C., 2017. Mitigation of whistling in vertical corrugated pipes by liquid addition. Exp. Fluids 58 (9), 107.

Gilliland, E.R., Sherwood, T.K., 1934. Diffusion of vapors into air streams. Indust. Eng. Chem. 26 (5), 516–523.

Glover, A.R., Skippon, S.M., Boyle, R.D., 1995. Interferometric laser imaging for droplet sizing: a method for droplet-size measurement in sparse spray systems. Appl. Opt. 34 (36), 8409–8421.

Gonzalez, R.C., Woods, R.E., 2012. Digital Image Processing. Prentice Hall.

Häber, T., Gebretsadik, M., Bockhorn, H., Zarzalis, N., 2015. The effect of total reflection in PLIF imaging of annular thin films. Int. J. Multiph. Flow 76, 64–72.

Hay, K.J., Liu, Z.-C., Hanratty, T.J., 1996. Relation of deposition to drop size when the rate law is nonlinear. Int. J. Multiph. Flow 22 (5), 829–848.

Hewitt, G.F., 1965. The breakdown of the liquid film in annular two-phase flow. Int. J. Heat Mass Transf. 8 (5), 781–791.

Ishii, M., Grolmes, M.A., 1975. Inception criteria for droplet entrainment in two-phase concurrent film flow. AIChE J. 21 (2), 308–318.

Ishii, M., Mishima, K., 1989. Droplet entrainment correlation in annular two-phase flow. Int. J. Heat Mass Transf. 32 (10), 1835–1846.

Kim, H.Y., Koyama, S., Matsumoto, W., 2001. Flow pattern and flow characteristics for counter-current two-phase flow in a vertical round tube with wire-coil inserts. Int. J. Multiph. Flow 27 (12), 2063–2081.

Koschatzky, V., Westerweel, J., Boersma, B.J., Scarano, F., Moore, P.D., 2011. High speed PIV applied to aerodynamic noise investigation. Exp. Fluids 50 (4), 863–876.

Kukreja, R.T., Lau, S.C., McMillin, R.D., 1993. Local heat/mass transfer distribution in a square channel with full and v-shaped ribs. Int. J. Heat Mass Transf. 36 (8), 2013–2020.

Kumar, R., Gottmann, M., Sridhar, K.R., 2002. Film thickness and wave velocity measurements in a vertical duct. J. Fluids Eng. 124 (3), 634–642.

Leutheusser, H.J., 1964. Flow nozzles with zero beta ratio. J. Basic Eng. 86 (3), 538–540.

Lide, D.R., 1994. CRC Handbook of Chemistry and Physics, 75 CRC press.

Pan, L., Hanratty, T.J., 2002. Correlation of entrainment for annular flow in vertical pipes. Int. J. Multiph. Flow 28 (3), 363–384.

Sawant, P., Ishii, M., Hazuku, T., Takamasa, T., Mori, M., 2008. Properties of disturbance waves in vertical annular two-phase flow. Nucl. Eng. Des. 238 (12), 3528–3541.

Sawant, P., Ishii, M., Mori, M., 2009. Prediction of amount of entrained droplets in vertical annular two-phase flow. Int. J. Heat Fluid Flow 30 (4), 715–728.

Schubring, D., Ashwood, A.C., Shedd, T.A., Hurlburt, E.T., 2010. Planar laser-induced fluorescence (PLIF) measurements of liquid film thickness in annular flow. part i: methods and data. Int. J. Multiph. Flow 36 (10), 815–824.

Taitel, Y., Bornea, D., Dukler, A., 1980. Modelling flow pattern transitions for steady upward gas-liquid flow in vertical tubes. AIChE J. 26 (3), 345–354.

Turner, R.G., Hubbard, M.G., Dukler, A.E., 1969. Analysis and prediction of minimum flow rate for the continuous removal of liquids from gas wells. J. Pet. Technol. 21 (11), 1–475.

Wallis, G.B., 1968. Phenomena of liquid transfer in two-phase dispersed annular flow. Int. J. Heat Mass Transf. 11 (4), 783–785.

van 't Westende, J.M.C., Kemp, H.K., Belt, R.J., Portela, L.M., Mudde, R.F., Oliemans, R.V.A., 2007. On the role of droplets in cocurrent annular and churn-annular pipe flow. Int. J. Multiph. Flow 33 (6), 595–615.

Zabaras, G., Dukler, A.E., Moalem-Maron, D., 1986. Vertical upward cocurrent gas-liquid annular flow. AIChE J. 32 (5), 829–843.